First investigation of quartz and calcite shape fabrics in strained shales by means of X-ray tomography

Hugo Saur, Pascale Sénéchal, Tiphaine Boiron, Charles Aubourg, Hannelore Derluyn, Peter Moonen

First investigation of quartz and calcite shape fabrics in strained shales by means of X-ray tomography

H. Saur[1*], P. Sénéchal[2], T. Boiron[1], C. Aubourg[1], H. Derluyn[1], P. Moonen[1,2]
[1] CNRS/ Total/ Univ Pau & Pays Adour/ E2S UPPA, Laboratoire des Fluides Complexes et leurs Réservoirs-IPRA, UMR5150, 64000, Pau, France
[2] CNRS/ Univ Pau & Pays Adour/ E2S UPPA, Développement des Méthodologies Expérimentales-IPRA, UPS3360, 64000, Pau, France
*corresponding author: hugo.saur@univ-pau.fr

Highlights:

- Fine-grained rock fabric is investigated by X-ray tomography and SEM-EDS.
- Samples cover all stages of cleavage development along a strain gradient.
- Shape preferred orientation of quartz, calcite and pores is studied.
- Deformation imprints differently on the grain shape fabric of quartz and calcite.
- Grain fracturing, rotation and pressure-solution identified as dominant processes.

Keywords: High resolution XCT, calcareous shale, cleavage, shape preferred orientation, quartz, calcite

Abstract

We document the evolution of the 3D fabric of shale along a km-long strain gradient in the Jaca basin (Southern Pyrenees, Spain). With respect to the distance from a thrust, samples were collected in the cleavage-free domain, at the onset of the pencil-cleavage domain, within the pencil-cleavage domain and within the slaty-cleavage domain. By combining high resolution X-ray computed tomography (XCT) and energy dispersive X-ray spectroscopy (EDS), the morphology and the Shape Preferred Orientation (SPO) of thousands of quartz grains, calcite grains and pores was studied. In the least deformed samples, quartz and calcite display mean foliation parallel to bedding with comparable dispersion. In the pencil-cleavage domain, quartz foliation still follows the bedding while calcite foliation is mostly governed by cleavage. In the slaty-cleavage domain, calcite shows a much better organization, with foliation parallel to cleavage, mimicking closely the pore fabric. By contrast, the quartz shape fabric is much less defined, scattered between bedding and cleavage planes. This suggests that quartz grain act as rigid marker in the ductile matrix, while calcite grain orientation is governed by dissolution-precipitation processes.

1 Introduction

The fabric of fine-grained rocks is commonly studied by means of optical microscopy, electron-imaging techniques (Secondary Electron Microscopy and Transmission Electron Microscopy) or X-ray diffraction techniques. These techniques have been used to determine the evolution of the

phyllosilicate fabric and the main deformation mechanisms of these platy minerals along a strain gradient in the transition from mudstone to slate at Lehigh gap, Pennsylvania (Lee et al., 1986; Ho et al., 1995; van der Pluijm et al., 1998). While imaging techniques can provide 2D shape fabrics of grains, the X-ray diffraction techniques, such as the X-ray pole figure goniometry (Oertel, 1983; van der Pluijm et al., 1994) and high-energy synchrotron X-rays (Wenk et al., 2007), aim mostly at determining the lattice-preferred orientation (LPO) of phyllosilicates in these rocks. Another powerful technique to determine the fabric of deformed fine-grained rocks is the Anisotropy of Magnetic Susceptibility or AMS (Tarling & Hrouda, 1993; Borradaile & Jackson, 2004; Parés, 2015). The AMS provides a bulk magnetic fabric, through a magnetic susceptibility tensor, retracing the preferred orientation (shape or magnetocrystalline) of both ferromagnetic, diamagnetic and paramagnetic minerals. In the case of mudrocks, paramagnetic minerals (i.e. phyllosilicates) are generally the main contributors to the AMS signal and the magnetic fabric often reflects the clay fabric (Hirt et al., 2004; Parés, 2015). Using AMS and other magnetic analyses, Hirt et al. (2004); Housen & van der Pluijm (1991) proposed deformation mechanisms associated to slaty cleavage development in a fine-grained matrix at Lehigh gap. However, little attention has been given to other shale bearing minerals such as quartz and calcite and information on the 3D shape fabrics of these common minerals in gradually deformed pelitic rocks is scarce.

Shape fabrics or Shape Preferred Orientation (SPO) determination of grains can be done thanks to numerous techniques. As mentioned, AMS can provide the SPO of ferromagnetic minerals such as magnetite if they are the main magnetic carriers in the rock matrix. Other techniques mostly rely on 2D (digital) image analysis and we can cite the intercept counting method (Launeau et al., 1990, 2010; Launeau & Robin, 1996), the wavelet transformation (Gaillot et al., 1999) and the autocorrelation function (Heilbronner, 1992; Pfleiderer & Halls, 1993). More recently, Thissen & Brandon (2015) have developed a method to estimate rock fabric and to evaluate the strain using the autocorrelation function on 3D X-ray computed tomography data. Generally, to obtain 3D information from 2D image analysis only, three orthogonal pictures of outcrop microstructures, images of thin sections or polished surfaces are combined. It refers to the discipline of stereology (Underwood, 1970). This technique has been successfully applied by Grégoire et al. (1998); Launeau & Cruden (1998) and by Hastie et al. (2011, 2013) in igneous rocks. It is however desirable to obtain a 3D characterization of SPO of rock constituents in a faster and non-destructive way and for this purpose X-ray tomography is particularly appealing.

X-ray computed tomography (XCT) is now a well-established, powerful and non-destructive method to investigate the microstructure of rocks in three dimensions (Ketcham & Carlson, 2001; Ketcham,

2005; Carlson, 2006; Baker et al., 2012; Cnudde & Boone, 2013). The advantage of this imaging technique relies on its ability to provide the 3D shape fabric, for each individual object (grain or pore space) and makes the quantitative analysis statistically robust. The study of SPO of minerals by laboratory XCT or synchrotron XCT has proven to be valuable within various coarse-grained materials (Ketcham, 2005; Zucali et al., 2014; Sayab et al., 2015, 2017; Kahl et al., 2017) but also in fine-grained sedimentary rocks (Kanitpanyacharoen et al., 2012; Wenk et al., 2017). XCT does not measure the chemical composition of a rock sample but reflects the density and atomic number of its components. However, chemical identification can be performed by taking account of differences at elemental absorption edges, with synchrotron X-rays (Gualda et al., 2010) or by using a lab-based instrument equipped with a spectroscopic imaging detector (Egan et al., 2015). Recently, phase-contrast (holo-)tomography, X-ray fluorescence tomography and X-ray diffraction were used together in order to study chemical features of zircons (Suuronen & Sayab, 2018). Otherwise, laboratory XCT can be easily combined with other techniques, such as energy dispersive X-ray spectroscopy (EDS), to determine the chemical nature of rock constituents. This 2D-3D registration method has been commonly used in studies related to the characterization of reservoir rocks (Golab et al., 2010, 2013; De Boever et al., 2015) but also in metamorphic studies (Macente et al., 2017). Because of its accessibility, simplicity and quick implementation, we chose to use EDS to supplement information from lab-based X-ray absorption-contrast images.

Here we propose a novel methodology to study the shape fabric of common shale-bearing minerals (quartz, calcite), but also pore spaces, in three dimensions by combining of XCT and EDS. The proposed method is then applied to study deformed shales from the South Pyrenean foreland. Results demonstrate that the shape fabric of quartz and calcite exhibit a contrasting evolution along a km-long strain gradient. The purpose of this work is however not to go through details about the geological setting but more to emphasize the usefulness of the method that can be applied on fine-grained rocks in various geological context.

2 Geological setting and sampling

The Jaca basin is a piggyback basin of the South Pyrenean foreland, incorporated in the Pyrenean Orogeny from the Eocene to the Early Miocene (Labaume et al., 1985; Hogan & Burbank, 1996; Izquierdo-Llavall et al., 2013; Crognier et al., 2018). The Northern part of the Jaca Basin is made up of the Hecho turbiditic group. The Sierra de Leyre (Fig. 1a) bounds the southern part of the Hecho group. We focus on the Hecho Marls Formation (Eocene), which outcrop near the Sigües locality, and more precisely on the footwall of a steep thrust, which delineates the southern anticline of the Sierra de Leyre. The bedding (S0) of Hecho marls is sub-horizontal (Fig. 2a), except at few meters from the

emerged thrust, where footwall syncline developed, marked by overturned bedding dipping to the North (Fig. 2e).

In this study, we observed a strain gradient associated to cleavage development (S1) north of Sigües, correlated to the distance from the thrust. Cleavage develops as axial planes parallel to the major folds axes (mostly oriented N100o) but damage is induced by thrust propagation. At ~2 km south from the emerged thrust, there is no cleavage, and shales are only affected by a fracture network (Crognier et al., 2018). We refer to this type of petrofabric, corresponding to a low strain area, as "cleavage-free" throughout the text. In this domain, bedding has a dip of 15° towards the South (Fig. 2a). In the range ~1 km-0.5 km from the thrust, a pencil cleavage develops, dipping to the North and oblique to the bedding. The spacing between cleavage planes is metric at ~1 km and evolves gradually to millimetric at ~0.5 km. We refer to this petrofabric, corresponding to an intermediate strain area, as "pencil-cleavage". In this study, the bedding is still well observed in the pencil-cleavage domain (Fig. 2b-c). The dip of the bedding is 10° towards the South. At a distance below 0.5 km from the thrust, the cleavage intensity increases and the cleavage spacing becomes infra millimetric. We refer to this petrofabric, corresponding to a high strain area, as "slaty-cleavage". Here cleavage is strongly oblique to a horizontal bedding (Fig. 2d). Continuing towards the North, the bedding is now barely detectable and the change between sub-horizontal to overturned beds is difficult to observe near the thrust. The slaty cleavage, strongly dipping to the North, superimposes the bedding that has a dip of 60° towards the North forming a transposition structure (Fig. 2e). This is the slaty-cleavage domain where cleavage and bedding are nearly parallel due to high strain. The Sigües site exhibits therefore an exceptional exposure where it is possible to monitor, meter by meter, the evolution of a fine-grained sedimentary matrix in response to cleavage development.

In this study, five calcareous shale samples (A1, A2, A3, A4, A5) have been collected from the South to the North, with respectively a cleavage-free petrofabric (A1, 1.95 km from thrust), an incipient pencil-cleavage petrofabric (A2, 0.95 km), a pencil-cleavage petrofabric (A3, 480 m) and two slaty cleavage petrofabrics (150 and 15 m for A4 and A5 respectively). For the A4 sample, the bedding is sub-horizontal, superimposed by a steep cleavage. For the A5 sample, located near the thrust in the footwall syncline, overturned bedding and cleavage are nearly parallel due to the transposition of the two structures.

3 Methods

3.1 Workflow

The complete acquisition workflow applied in this study is described in Fig. 3. The workflow includes:

1) Extraction of a drill core from a georeferenced cylindrical field sample. A 'T' shaped orientation marker respecting the strike of the field sample is reported on the top of the extracted drill core (Fig. 3a).
2) Performing a first X-ray tomographic acquisition of the drill core. Image processing enables to extract different phases corresponding to shale constituents (Fig. 3b).
3) Polishing the drill core in the longitudinal direction (Fig. 3c).
4) Performing an EDS analysis on this polished surface (Fig. 3d),
5) Performing a second X-ray tomographic acquisition permitting to position the 2D EDS dataset within the 3D X-ray data set of the entire drill core and to fuse the data (Fig. 3e).

The following sections shortly present the principles of XCT and EDS and describe more precisely how the data fusion is performed and how it enables to perform detailed shape fabric analysis.

3.2 High resolution X-ray computed tomography

3.2.1 Acquisition and reconstruction of data

Laboratory X-ray computed tomography (XCT) is a technique, which enables inner inspection of a sample at high resolution and in a non-destructive way. The sample is placed between a source and a detector. During an acquisition, a conical X-ray beam illuminates the sample and a series of 2D projection images are recorded for various sample orientations. The pixel values of each of these images correspond to the intensity of the transmitted X-ray beam and depend on the attenuation of the sample material (Ketcham & Carlson, 2001; Ketcham, 2005; Baker et al., 2012). The attenuation is function of the density and the atomic number of the material and of the incident X-ray spectrum (Ketcham & Carlson, 2001; Baker et al., 2012). The recorded dataset of 2D projection images is subsequently converted into a three-dimensional dataset in which every voxel (i.e. a pixel in 3D) reflects the average attenuation of the physical material located at that voxel position. As attenuation coefficients are material-specific, different mineral phases yield different grey values in the reconstructed 3D images. Analysis of the spatial distribution of the reconstructed images hence permits to determine the geometry and location of the mineral phases. Attenuation-based X-ray tomography however does not provide crystallographic information nor direct chemical information.

In this work, five shale drill cores (A1-A5) were scanned with a Zeiss Xradia Versa 510 X-ray tomograph at DMEX (UPPA). This tomograph combines geometric and optical magnification, enabling the acquisition of high-resolution images for relatively large sample sizes. The 16-bit CCD detector is capable of acquiring radiographs with 2048^2 pixels. The acquisition parameters are selected in view of optimizing the image contrast, the signal-to-noise ratio and the acquisition

duration (Table 1). The set of recorded radiographs are reconstructed with XRM Reconstructor® (Zeiss, version 11) in order to obtain a stack of cross-sections forming a digital volume of the sample. This reconstruction software is based on the standard filtered back projection algorithm (Ramachandran & Lakshminarayanan, 1971).

Table 1: sample parameters of X-ray tomography (XCT) for each studied sample.

Sample	A1	A2	A3	A4	A5
Diameter (mm)	2.5	1.9	1.8	1.8	1.8
Field of View (mm)	2.9	2.5	1.95	2.35	2.35
Acceleration tension (kVp)	50	50	40	40	40
Target current (µA)	80	80	75	75	75
Power (W)	4	4	3	3	3
Exposure time (s)	18	12	40	40	40
Number of projections	2001	2001	2001	1601	1601
Voxel size (µm)	1.5	1.3	1.0	1.2	1.2
Total acquisition time (hours)	12	8.5	24	22	22

3.2.2 Data processing

The XCT data were processed, visualized and interpreted using Avizo® (FEI, Version 9.0.0). A two-step image processing is applied to the data. In a filtering step the signal-to-noise ratio is improved. The subsequent segmentation step enables extracting mineral phases and pore spaces for further quantitative analysis in 3D. Note that for each sample, image processing is done for a subvolume (volume of interest) located in the central part of the image (Fig. 3f) as the structure near edges of the drill core might be affected by the coring.

3.2.2.1 Filtering

The noise in the reconstructed XCT dataset can be reduced by applying pre-processing filters which are mathematical algorithms that act on each pixel or voxel of the image (Kaestner et al., 2008; Russ et al., 2015). The aim of the filtering process is to make the interpretation of the image easier by increasing the contrast between the objects (Kaestner et al., 2008; Russ et al., 2015). In our study, an anisotropic diffusion filter proposed by Bernard et al. (2011) is applied to each dataset. This filter is a modified version of the classical anisotropic diffusion filter (Perona & Malik, 1990). It smoothens noisy but relatively uniform regions of the image (i.e. each individual phase), while preserving the boundaries between the phases (i.e. the contours of the objects). Additionally, the Despeckle module is applied to remove residual noise based on a mean calculation of neighborhood voxels values.

3.2.2.2 Segmentation

Segmentation enables to partition the image into regions so that each region is homogeneous with regard to certain properties, such as gray level or texture (Dougherty, 1994). Here, it is sought to extract five phases which are associated to different gray levels ranging from black (lowest X-ray attenuation, phase 1) to white (highest X-ray attenuation, phase 5) (Fig. S1). In the case of fine-grained sedimentary rocks, the structure of the rock is complex due to various sized minerals of different densities and a multi-scale porosity. Indeed, porosity varies over a wide range of length scales in shales and can only be fully characterized using multi-scale imaging techniques. Consequently, the histogram of the gray levels shows overlapping values that make it difficult to distinguish each phase. The comparison of results obtained by different methods of thresholding shows that global manual thresholding is the most suitable in this context. Morphological filters (Serra & Vincent, 1992; Dougherty, 1994) have also been applied as post-segmentation image processing, when it was necessary, to discriminate two phases and to reduce misclassification errors near phase interfaces (Fig. S1). The thresholds are chosen to dissociate the different phases and to respect their boundaries. As this choice could be considered as subjective, upper and lower bounds on the thresholds are determined that encompass all reasonable choices of an experienced operator. These permit to assess the uncertainties on the volume of each phase from ±15% to ±5% depending on the considered phase. Once the tomographic phases have been segmented (Fig. 3b), we desire to identify them chemically using EDS.

3.3 Energy-Dispersive X-ray Spectroscopy

Energy dispersive X-ray spectroscopy (EDS) enables acquiring a chemical map at nanometer resolution of the elements from Li to U situated on the analyzed surface. Associated with SEM devices, EDS uses X-rays generated by the interaction of an electron beam with a sample to characterize the elemental composition (Goldstein et al., 2018).

In this work, we use EDS in a qualitative approach to identify the major constituents of the shale samples. A grid of scanning electron microscopy (SEM) and energy-dispersive X-ray spectroscopy (EDS) images is acquired to compose a chemical map of a plane surface obtained after the core has been polished in the longitudinal direction (Fig. 3c-d). SEM-EDS data acquisition is performed at the Raimond Castaing Microanalysis Centre (Toulouse, France). SEM images are collected as backscattered electrons (BSE) with a JEOL JSM-7800F Prime equipped with a Silicon Drift Detector from Oxford Instruments to generate the EDS images. The acceleration voltage used for our study is

10 kV. One EDS map is obtained for each detected chemical element. Two samples (A1 and A2) are characterized to identify major constituents of the rock, EDS parameters are summarized in Table S1. SEM images are not used in this work because they are redundant with the X-ray dataset.

3.4 Image registration and fusion

Registration of the EDS images and the XCT volume is done in order to propagate chemical identification given by EDS images into the whole XCT volume. First, the registration of the initial XCT image with the final XCT image after polishing is performed. This operation is essential to precisely locate the surface analyzed by EDS inside the initial XCT volume. The Mutual Information method from Avizo® is used to register these datasets and the plane that corresponds to the polished surface is extracted from the initial volume. This plane and the EDS image are not strictly superimposable because they are not exactly parallel, nor do they have the same resolution. Furthermore, the EDS image integrates information over a thickness of several microns. Therefore, we fine-tune the registration based on landmarks (i.e. characteristic features in the image).

Four out of five XCT phases can be directly associated to a mineral, namely quartz, clayey matrix, calcite and pyrite for phases two to five, respectively. Light elements cannot be detected by EDS, and therefore phase 1 (lowest X-ray attenuation) can be associated with the air-filled pores of the material. This procedure enables propagating the chemical information from 2D EDS maps to the entire XCT volume and to subsequently perform a shape fabric analysis of each phase.

3.5 Shape fabrics analysis

The shape of each individual phase (grain or pore) corresponds to the distribution of its voxels in the three-dimensional XCT image. In our case, the shape is approximated by a best-fit ellipsoid (Fig. 3g) having the same moments of inertia as the original object (Jähne, 1997). The inertia matrix of each object is obtained by the calculation of the second-order moments. The diagonalization of the matrix provides three eigenvalues which correspond to the principal moments of inertia and the associated three orthogonal eigenvectors which correspond to the principal axes of inertia. The major, intermediate and minor eigenvectors give information on the spatial orientation of the object in the coordinate system of the sample. As the strike and dip of each sample is known, the local coordinate system can be converted into the geographic coordinate system. The shape of the object is

approximated by the eigenvalues, which are related to the best-fit ellipsoid's semi-axes. Truncated objects placed at the edges of the volume were excluded, as they would bias the shape-analysis.

The shape of each object is further characterized by three non-dimensional shape parameters, namely anisotropy, elongation and flatness.

- The anisotropy is defined by $1 - e_3/e_1$ where e_3 and e_1 are the smallest and largest eigenvalues of the inertia matrix respectively. A spherical object has anisotropy equal to zero.
- The elongation is defined by e_2/e_1 where e_2 and e_1 are the medium and largest eigenvalues respectively.
- The flatness is defined by e_3/e_2 where e_3 and e_2 are the smallest and medium eigenvalues respectively.

4 Results

4.1 General observations

4.1.1 Distribution of phases

The results concerning quartz, calcite and pores phases are provided in this work. The study of the phyllosilicate matrix is discarded because of insufficient XCT resolution while the study of pyrite is outside the scope of this paper. The number of objects belonging to each phase (calcite, quartz and pore spaces) and their relative abundance in the volume of interest of the samples are reported in Table 2. In this study, objects under 729 µm^3 (corresponding to 216 voxels in A1, 332 voxels in A2, 729 voxels in A3, 422 voxels in A4 and A5) are considered as noise and are eliminated. Thus, the volumetric contribution of each phase obtained with XCT underestimates the real quantity present in the samples to some extent. All together, the three phases represent 3.5 to 7.6% of the volume of interest. In comparison, the rock matrix represents around 92.4 to 96.5%. We thus focus on a small fraction of the rock volume (Table 2). The volume distribution of the objects ranges from 729 to near $2*10^6$ µm^3 for the biggest calcite grains. Nevertheless, among each mineralogical phase (quartz and calcite), around 95% of the studied particles have a size ranging from 729 to 20729 µm^3. The respective distributions, in the five samples, of quartz and calcite ranging from 729 to 20729 µm^3, are represented in Fig. S2 and show a remarkable similarity.

Table 2: Volume of interest for each sample. Number and volume fraction of quartz, calcite and pores particles in this volume, obtained after segmentation.

Sample	A1	A2	A3	A4	A5
Volume of interest (mm^3)	6.12	2.10	1.76	2.34	2.15
Number of quartz grains	13,451	5,282	13,109	8,311	7,371
Volume fraction of quartz (1)	1.63 %	1.48 %	2.92 %	2.07 %	1.74 %

Number of calcite grains	15,932	9,950	15,610	13,324	12,938
Volume fraction of calcite (2)	1.82 %	4.27 %	3.17 %	5.35 %	5.04 %
Number of pores	435	277	104	1,500	713
Volume fraction of pores (3)	0.065 %	0.023 %	0.009 %	0.134 %	0.372 %
(1)+(2)+(3)	3.52 %	5.77 %	6.10 %	7.55 %	7.15 %

307

308 **4.1.2 Description of the XCT images**

309

310 Fig. 4 presents a vertical north-south cross section through each sample, illustrating the horizontal
311 bedding orientation from A1 to A4, the appearance of a cleavage plane from A3 onwards, as well as
312 the rotation of this plane from A3 to A5. As the depicted cross-section intersects each cylindrical
313 sample in an oblique fashion, the shapes of the cross-sections differ from one sample to the next.
314 Images in the samples reference frame are available in Fig. S3.
315 Fig. 4 shows that most of the calcite grains are rounded shaped and correspond to microfossils and
316 shell fragments. On the contrary, quartz grains are more angular. At this micron scale, we observe a
317 preferred alignment of grains in the least deformed samples (A1 and A2). This fabric is attributed to
318 bedding as this planar structure is sub-horizontal, which is in accordance with field observations. In
319 sample A3, a secondary planar fabric becomes slightly visible, it corresponds to cleavage that cross-
320 cut bedding structures at low angle. Cleavage domains are subtle in this XCT image, sometimes
321 marked by preferred alignment of calcite bioclasts and spaced by more than 1 mm in this sample. In
322 samples A4 and A5, the traces of cleavage domains are deduced from high porosity surfaces, which
323 appear as microcracks in the XCT images (see Fig. S3 for more images). Because clay minerals are
324 known to concentrate in cleavage domains (seams), clays may have dehydrated during storage of the
325 samples and formed microcracks. From these structures, we can infer the presence of pressure
326 solution seams. Furthermore, the calcite bioclasts are often truncated by the seams and confirm that
327 pressure solution has been responsible of the growth of these surfaces (Engelder & Marshak, 1985;
328 Passchier & Trouw, 2005). The truncation of calcite by pressure solution seams is supported by optical
329 microscopy observation (Fig. 5). The cleavage domains are more penetrative in A5 than in A4.
330 Average spacing between cleavage domains is of 212 µm ± 65 µm in A4 and of 116 ± 16 µm in A5.
331 However, the measure of the spacing of cleavage depends on the scale of observation and the true
332 spacing is certainly less than these values. In our case, spatial resolution depends on the voxel size of
333 the XCT images. In A4, the seams are discontinuous, subparallel to slightly anastomose around grains
334 and rather rough. In A5, the seams appear discontinuous, subparallel and smoother. In both samples
335 A4 and A5, grains within or close to the cleavage domains are strongly aligned, parallel to the seams.
336 In between the cleavage domains of A4, grains are whether subparallel, orthogonal (related to the
337 bedding fabric) or randomly oriented. In between the cleavage domains of A5, calcite grains are
338 mostly aligned parallel to seams giving a strong planar fabric to the rock. Quartz grains are rather

randomly oriented in A5. We remark that cleavage domains are heterogeneously spaced in A4 compared to cleavage domains in A5, which are equally spaced throughout the rock volume.

4.2 Grain and pore spaces shape.

At first glance, the distribution of the shape parameters of quartz, calcite and pores highlights a global transition towards more anisotropic, more elongated and flatter objects from the cleavage-free domain (A1) to the slaty-cleavage domain (A5) (Fig. 6). However, the evolution of the shape parameters is not the same for each phase.

Concerning the quartz (Fig. 6), the major shift in distributions of both anisotropy, elongation and flatness takes place between A1 and A2. After what, the distribution of these parameters is not really distinguishable between samples A2, A3, A4, A5. However, we should note that distributions in A3 feature the most anisotropic, elongated and flattened quartz grains.

Concerning the calcite (Fig. 6), there is a regular shift of the distribution of the three parameters from A1 to A5. As strain increases, calcite grains gradually become more deformed. This is particularly well illustrated by evolution of anisotropy and flatness. However, we should note that distributions of anisotropy and elongation in A3 are close to that in A5. The distribution of flatness in A3 is similar to that in A4. We should note that quartz and calcite have similar distributions of anisotropy, elongation and flatness in A1 and A2.

Concerning the pore spaces (Fig. 6), the distribution of anisotropy and flatness are delicate to interpret due to a high proportion of very anisotropic and flattened pores in A1 and A5. These pores may in fact correspond to microcracks present in A1 and A5. Elongation of the pore spaces is similar for the five samples.

As significant results, we thus retain common shape features of quartz and calcite grains in samples A1 and A2, the change of quartz shape between A1 and A2 solely, contrasting with the continuous and regular evolution of calcite shape across the five samples. We also note that quartz grains seem to be more deformed in sample A3. It has been verified that the specific segmentation thresholds (cf. segmentation paragraph) for each phase have no influence on the evolution of shape parameters.

4.3 Shape preferred orientation of quartz, calcite and pores.

We plot density contours of the short (L3) and long (L1) axes corresponding to thousands of objects (grains, pore spaces) in equal area and lower hemisphere projections representing a geographic coordinate system (North-East-Down) (Fig. 7-8), using the OpenStereo software (Grohmann & Campanha, 2010). In fabric analysis, it is generally common to assign L3 as the pole of foliation (Fig. 7) and L1 as the lineation (Fig. 8). Poles of the bedding and cleavage planes measured on the XCT images from the alignment of grains (Fig. 4) are also reported onto these stereographic plots in a common geographic coordinate system (North-East-Down).

In the cleavage-free domain (sample A1), all objects display foliation parallel to the bedding plane (Fig. 7). Pore spaces are well-organized with a maximum density near 30% around the pole of bedding. Quartz and calcite display almost the same degree of dispersion and have maximum densities coinciding with the pole of bedding (3.5% and 3.8% respectively, which mean 3.5%/1% area and 3.8%/1% area respectively). Lineation of individual ellipsoid long axes (L1) spread sub-horizontally in the bedding plane with a slight NW-SE trend (Fig. 8). At the onset of the pencil-cleavage domain (sample A2), all poles of foliation spread near the bedding pole. Here again, quartz and calcite have similar maximum densities (3.3% and 3.7% respectively). Poles of the pores are more disorganized. No evident lineation is observed but we can notice a slight preference towards NW-SE for quartz and calcite (Fig. 8). Lineation is related to bedding. In the pencil-cleavage domain, where cleavage is oblique to bedding (sample A3), we observe notable differences. Quartz displays a scattered foliation related to the bedding pole with a maximum density of 2.2% (Fig. 7). Calcite shows a NNE-SSW directed girdle of the pole of foliation between the pole of cleavage and the pole of bedding. However, calcite foliation mostly indicate a cleavage related fabric with a maximum density of 3.0% around the pole of cleavage. The pole of foliation of pore spaces seems to be scattered between the pole of cleavage and the pole of bedding. The lineation is sub-horizontal and related to bedding for quartz grains but still displays a preference towards NW-SE as in A1 and A2 (Fig. 8). As of now, the lineation tends ESE-WNW for calcite grains and correspond to an intersection lineation of bedding and cleavage planes. Calcite lineation also displays incipient contours in the cleavage plane. The lineation of pore spaces cannot be assessed. In the slaty cleavage domain, where cleavage is strongly oblique to bedding (sample A4), we also observe notable differences. Quartz displays a N-S directed girdle of the pole of foliation between the pole of cleavage and the pole of bedding (Fig. 7). Quartz grains are thus influenced by these two planes. In contrast, calcite grains and pore spaces have a well concentrated foliation near the pole of cleavage. At this strain state, quartz and calcite show different maximum densities around the pole of cleavage, 2.3% for quartz compared to 6.6% for calcite. The lineation tends slightly E-W for quartz, close to an intersection lineation (Fig. 8). For calcite and pore spaces, the intersection lineation mostly lies E-W sub-horizontally but is also

depicting the cleavage great circle with some steep lineations within the cleavage plane. In the slaty-cleavage domain, where bedding and cleavage are parallel to each other (sample A5), all foliation poles are grouped parallel to the bedding/cleavage pole (Fig. 7). However, quartz foliation is still quite disorganized and show a weak maximum density of 2.9%. Maximum density at the pole of cleavage reaches 11.4% for calcite foliation. The dispersion of the quartz foliation may indicate that bedding and cleavage planes are not exactly parallel. The pole of foliation of pores is well defined and displays a maximum density of 38.2%. The lineation is relatively scattered, sub-horizontal in trend for quartz but also with a girdle around the dip of the cleavage plane (Fig. 8). Calcite and pore spaces display a down-dip stretching lineation with a maximum density of 4.0% and 7.0% respectively. We should note as a general trend that foliation of grains and pore spaces is better defined than their lineation.

5 Discussion

Results of this microscale study are fully consistent with field data. Cleavage development along the strain gradient is well recorded in XCT images and is demonstrated by our microstructural approach on quartz, calcite and pores. Although we have worked on a small rock volume (volume of interest between 1 to 6 mm^3), results are well correlated to field observations and show clear trends, indicating that the samples are representative. The representativeness of sample is also illustrated by the volume distribution remarkably similar for calcite and quartz, independently of strain. Moreover, the amount of investigated objects from XCT data of each sample (~10000 for quartz and calcite, more than 100 for pores) makes the study statistically robust.

In the cleavage-free domain (A1), quartz and calcite have similar shape features (Fig. 6) and SPO (Fig. 7-8-9). In these shales, quartz grains may mostly be provided by detrital inputs whereas calcite grains may be provided by carbonates pelagic particles. Grain shape may result from compaction both during burial/diagenesis and tectonic compression. SPO of quartz and calcite is governed by a typical bedding-parallel fabric with short axis L3 normal to the bedding plane and no specific orientation of the long axis L1 (Fig. 7). SPO of pores is also governed by the bedding.

At the onset of pencil-cleavage domain (A2), we observe similar shape features (Fig. 6) and SPO (Fig. 7-8-9) for quartz and calcite but they have evolved with respect to the undeformed sample A1. Particles are more deformed (Fig. 6) but their foliation remains close to the pole of bedding, lineation is almost the same as in A1. No specific change in SPO is recorded in this low strain intensity area.

Grain shape may change due to microfracturing, as illustrated in Fig. 10. Evolution of grain shape and SPO is reported in a sketch presented in fig. 10 that follows this discussion.

In the pencil-cleavage domain (A3), where cleavage is oblique to the bedding orientation, shape features and SPO differ between quartz and calcite. Quartz and calcite grains are more deformed in this sample as shown by the distribution of shape parameters (Fig. 6). Quartz SPO is still related to bedding but disturbed (Fig. 7-8-9). Calcite SPO is developing a cleavage foliation and is depicting an intersection lineation. Some calcite grains might still be related to the bedding as described by the girdle of L3. The fabric of pore spaces in this sample is more difficult to interpret because of the weak number of pore spaces. Mechanical rotation, pressure-solution and new crystallization of phyllosilicates grains have been commonly proposed as the major processes acting during cleavage development associated to the transition from mudstones to shales and slates (Engelder & Marshak, 1985; Lee et al., 1986; Ho et al., 1995, 1996; Passchier & Trouw, 2005). van der Pluijm et al. (1998) discussed the possible roles of thermal and strain energy in determining which process dominates. Generally, mechanical rotation is said to be the dominant process affecting detrital grains in early stages of cleavage development, as proposed by works on phyllosilicates grains (Ho et al., 1995, 1996; Hirt et al., 2004) and on magnetite grains (Housen & van der Pluijm, 1991). This would be consistent with our observations on the quartz and calcite grains in the pencil-cleavage domain. Changes in shape features and SPO of quartz and calcite may result from mechanical processes such as grain rotation. Alternatively, one could assume that grain rotation does not take place during deformation (Fig. 10), especially for grains located in between the cleavage domains. Since both scenarios are end-members in between we can find intermediate models that may explain the dispersion of the poles of foliation and low maximum densities. Brittle fracturing of grains may also erode grain contours and affect their shape. At this intermediate strain intensity, we cannot detect evidences for pressure-solution in the XCT image so we propose that grain rotation and grain fracturing are the dominant deformation processes to accommodate shortening. However, we do not exclude the play of pressure-solution. It is important to note that this strain state shows the weakest maximum densities of foliation and lineation which attest for the most disturbed shape fabrics of grains and pores.

In the slaty-cleavage domain (A4), where cleavage is strongly oblique to the bedding orientation, shape features and SPO differ between quartz and calcite. The shape of the quartz grains remains the same as in A2, while the calcite grains continue to deform (Fig. 6). The major step in the SPO evolution of grains is apparent in this sample and well demonstrated by differences in the maximum density of quartz and calcite foliations (Fig. 9). Quartz foliation is now related to poles of both

bedding and cleavage (Fig. 7). More precisely, one third of the total quartz grains keep a bedding influenced fabric in this sample, compared to calcite and pores particles which are strictly governed by cleavage. We have compared the shape of the quartz grain population related to both the pole of cleavage and the pole of bedding, by selecting particles having a dip above or under 45°, but no differences have been observed in their respective size distribution. Therefore, these different orientations are not related to the size of the quartz grains. In this sample, we have seen some evidence for pressure-solution such as and truncated calcite grains (Fig. 5 & Fig. S3). It should be noticed that in XCT data, truncated grain and its pressure shadows (tails) are assimilated as one grain because of equal densities, as opposed to what can be seen in optical microscopy. Furthermore, fine grains present in pressure shadows are beyond XCT image resolution. It explains the high degree of anisotropy of calcite grains obtained by XCT data processing which encompass many sub-micrometric grains to define one grain. In this sample, the increasing deformation of calcite grains and changes in their SPO could be explained by pressure-solution. We suppose that this process may be the reason of the divergent evolution of the shape features and SPO between quartz and calcite in A3 (Fig. 10). Pressure-solution may proceed on calcite grains but may be less effective or may not happen for quartz grains. It is well-known that pressure solution is a function of the thermodynamics conditions, especially temperature (Houseknecht, 1984; Bjorkum, 1996; Tournier, 2010), of the size and the composition of grains as well as of the stress conditions (Gratier et al., 2013). Another paramount parameter is the role of phyllosilicate in enhancing dissolution process of grains such as calcite and quartz (Dewers & Ortoleva, 1991; Renard et al., 1997; Meyer et al., 2006). More precisely, illite and mica are known to favor quartz dissolution in sandstones (Weyl, 1959; Houseknecht, 1988; Bjorkum, 1996; Tournier, 2010; Kristiansen et al., 2011). Even though both types of these phyllosilicates are present in our shales, the results of this study is not conclusive on their role in quartz dissolution. These shales have only experienced a peak temperature near 180°C (Izquierdo-Llavall et al., 2013) and we can propose that the thermodynamics conditions were prone to pressure-solution of calcite while they were not for quartz grains, or at least to a lesser extent. In particular, temperature may be the limiting parameter for quartz dissolution. It should be noticed that the distribution of the size of quartz and calcite (Fig. S2) remains similar in the five samples, which is particularly stunning considering the amount of strain recorded by the samples in the slaty-cleavage domain. It seems that even though calcite grains are affected by pressure-solution processes, these processes have no influence on the grain size. The grain shape evolves due to the processes mentioned above but the removed material is probably only redistributed and grain size remains stable.

In the slaty-cleavage domain (A5), where cleavage and bedding are parallel, shape features and SPO of quartz and calcite are still displaying differences. Quartz shows the same shape as in A2 and A3

while calcite becomes more strained (Fig. 6). Quartz SPO is mostly related to cleavage but still scattered both in terms of foliation and lineation (Fig. 7-8). Calcite and pores' foliation are governed by cleavage and are well defined. Calcite lineation, which is close to the dip of cleavage, may correspond to a stretching lineation. Evidences for pressure-solution on calcite grains are also highlighted in this sample A5 (Fig. 5 & Fig. S3). Thus, evolution of calcite shape and enhancement of its SPO at this strain state could be explained by pressure-solution (Fig. 10). Here also, quartz grains might not be affected by this process.

Information issued from textural analysis, e.g. by means of the electron backscatter diffraction (EBSD) technique, could complete this study. In particular, EBSD would provide more information on the type of grains (authigenic vs detrital) and their relations and overgrowths patterns for authigenic grains. This approach could also be completed and compared with the study of preferred orientation of matrix phyllosilicates at a higher resolution thanks to XCT synchrotron devices or the well-established X-ray texture goniometry. Also, the analysis of phyllosilicates and their interactions with quartz and calcite could be useful, to determine if they play a role in the pressure-solution process. Overall, this work offers new perspectives of investigations for the study of fine-grained rock fabric in 3D and in various geological contexts.

6 Conclusions

The combination of XCT and EDS data is a reliable and fast way to produce a three-dimensional chemical and structural characterization of a representative volume of a fine-grained rock sample at a micrometric scale. It is possible to identify the major rock constituents, to extract shape parameters and to gain insight in shape-preferred orientation of thousands of mineral grains and hundreds of pores. Therefore, investigating fine-grained rock fabric by means of XCT appears as a promising tool. According to this approach, we document for the first time the 3D shape fabrics of quartz and calcite and their evolution across a km-long strain gradient in the South Pyrenean foreland:

In five gradually more deformed calcareous shale samples (A1 to A5), we demonstrate that:

- quartz and calcite grains embedded in the matrix have analogous shape and SPO in the cleavage-free and at onset of pencil-cleavage domain (A1 and A2);
- quartz and calcite have distinct shape and SPO in the pencil-cleavage domain (A3) and in the slaty-cleavage domain (A4 and A5);
- pore fabric mimics calcite fabric along the strain gradient.

We envisage grain fracturing, grain rotation and pressure-solution as dominant processes acting in the matrix but affecting differently quartz and calcite. Quartz deformation may be mostly induced by grain fracturing and rigid rotation of grains and occurs preferentially in the first stages of cleavage development (onset of pencil-cleavage domain and pencil-cleavage domain). Detrital quartz grains could appear as rigid markers of strain. Calcite deformation may be favored by pressure-solution in the slaty-cleavage domain whereas it is not the case for quartz. Calcite could be a useful strain gauge as shown by its regular shape fabric evolution according to strain intensity.

Acknowledgments

The authors thank E2S UPPA for financially supporting the lead author of this article H. Saur, ISIFoR for financially supporting the reported field survey and the SEM-EDS analyses, as well as the company Total for providing UMS 3360 DMEX with the tomograph used to carry out the XCT acquisitions described in this article. We are grateful to the editor T. Takeshita and two reviewers for their helpful comments on the manuscript.

References

Baker, D. R., Mancini, L., Polacci, M., Higgins, M. D., Gualda, G. A. R., Hill, R. J., & Rivers, M. L. (2012). An introduction to the application of X-ray microtomography to the three-dimensional study of igneous rocks. *Lithos*, *148*, 262–276. https://doi.org/10.1016/J.LITHOS.2012.06.008

Bernard, D., Guillon, O., Combaret, N., & Plougonven, E. (2011). Constrained sintering of glass films: Microstructure evolution assessed through synchrotron computed microtomography. *Acta Materialia*, *59*(16), 6228–6238. https://doi.org/10.1016/J.ACTAMAT.2011.06.022

Bjorkum, P. A. (1996). How important is pressure in causing dissolution of quartz in sandstones? *Journal of Sedimentary Research*, *66*(1), 147–154. https://doi.org/10.1306/D42682DE-2B26-11D7-8648000102C1865D

Borradaile, G. J., & Jackson, M. (2004). Anisotropy of magnetic susceptibility (AMS): magnetic petrofabrics of deformed rocks. *Geological Society, London, Special Publications*, *238*(1), 299 LP – 360. https://doi.org/10.1144/GSL.SP.2004.238.01.18

Carlson, W. D. (2006). Three-dimensional imaging of earth and planetary materials. *Earth and Planetary Science Letters*, *249*(3–4), 133–147. https://doi.org/10.1016/j.epsl.2006.06.020

Cnudde, V., & Boone, M. N. (2013). High-resolution X-ray computed tomography in geosciences: A review of the current technology and applications. *Earth-Science Reviews*, *123*, 1–17.

https://doi.org/10.1016/J.EARSCIREV.2013.04.003

Crognier, N., Hoareau, G., Aubourg, C., Dubois, M., Lacroix, B., Branellec, M., Callot, J. P., & Vennemann, T. (2018). Syn-orogenic fluid flow in the Jaca basin (south Pyrenean fold and thrust belt) from fracture and vein analyses. *Basin Research*, *30*(2), 187–216. https://doi.org/10.1111/bre.12249

De Boever, W., Derluyn, H., Van Loo, D., Van Hoorebeke, L., & Cnudde, V. (2015). Data-fusion of high resolution X-ray CT, SEM and EDS for 3D and pseudo-3D chemical and structural characterization of sandstone. *Micron*, *74*, 15–21. https://doi.org/10.1016/j.micron.2015.04.003

Dewers, T., & Ortoleva, P. (1991). Influences of clay minerals on sandstone cementation and pressure solution. *Geology*, *19*(10), 1045–1048. https://doi.org/10.1130/0091-7613(1991)019<1045:IOCMOS>2.3.CO;2

Dougherty, E. R. (1994). *Digital image processing methods*. M. Dekker.

Egan, C. K., Jacques, S. D. M., Wilson, M. D., Veale, M. C., Seller, P., Beale, A. M., Pattrick, R. A. D., Withers, P. J., & Cernik, R. J. (2015). 3D chemical imaging in the laboratory by hyperspectral X-ray computed tomography. *Scientific Reports*, *5*, 15979. Retrieved from https://doi.org/10.1038/srep15979

Engelder, T., & Marshak, S. (1985). Disjunctive cleavage formed at shallow depths in sedimentary rocks. *Journal of Structural Geology*, *7*(3), 327–343. https://doi.org/https://doi.org/10.1016/0191-8141(85)90039-2

Gaillot, P., Darrozes, J., & Bouchez, J.-L. (1999). Wavelet transform: a future of rock fabric analysis? *Journal of Structural Geology*, *21*(11), 1615–1621. https://doi.org/https://doi.org/10.1016/S0191-8141(99)00073-5

Golab, A. N., Knackstedt, M. A., Averdunk, H., Senden, T., Butcher, A. R., & Jaime, P. (2010). 3D porosity and mineralogy characterization in tight gas sandstones. *The Leading Edge*, *29*(12), 1476–1483. https://doi.org/10.1190/1.3525363

Golab, A. N., Romeyn, R., Averdunk, H., Knackstedt, M., & Senden, T. J. (2013). 3D characterisation of potential CO2 reservoir and seal rocks. *Australian Journal of Earth Sciences*, *60*(1), 111–123. https://doi.org/10.1080/08120099.2012.675889

Goldstein, J., Newbury, D. E., Michael, J. R., Ritchie, N. W. M., Scott, J. H. J., & Joy, D. C. (2018). *Scanning electron microscopy and x-ray microanalysis*. New York, NY: Springer.

Gratier, J.-P., Dysthe, D. K., & Renard, F. (2013). Chapter 2 - The Role of Pressure Solution Creep in the Ductility of the Earth's Upper Crust. In R. B. T.-A. in G. Dmowska (Ed.), *Advances in Geophysics* (Vol. 54, pp. 47–179). Elsevier. https://doi.org/https://doi.org/10.1016/B978-0-12-380940-7.00002-0

Grégoire, V., Darrozes, J., Gaillot, P., Nédélec, A., & Launeau, P. (1998). Magnetite grain shape

615 fabric and distribution anisotropy vs rock magnetic fabric: a three-dimensional case study.
616 *Journal of Structural Geology*, *20*(7), 937–944. https://doi.org/10.1016/S0191-8141(98)00022-
617 4
618 Grohmann, C. H., & Campanha, G. A. (2010). OpenStereo: Open Source, Cross-Platform Software
619 for Structural Geology Analysis. *American Geophysical Union, Fall Meeting 2010, Abstract*
620 *Id. IN31C-06*. Retrieved from http://adsabs.harvard.edu/abs/2010AGUFMIN31C..06G
621 Gualda, G. A. R., Pamukcu, A. S., Claiborne, L. L., & Rivers, M. L. (2010). Quantitative 3D
622 petrography using X-ray tomography 3: Documenting accessory phases with differential
623 absorption tomography. *Geosphere*, *6*(6), 782–792. https://doi.org/10.1130/GES00568.1
624 Hastie, W. W., Watkeys, M. K., & Aubourg, C. (2011). Significance of magnetic and petrofabric in
625 Karoo-feeder dykes, northern Lebombo. *Tectonophysics*, *513*(1–4), 96–111.
626 https://doi.org/10.1016/J.TECTO.2011.10.008
627 Hastie, W. W., Watkeys, M. K., & Aubourg, C. (2013). Characterisation of grain-size, shape and
628 orientation of plagioclase in the Rooi Rand dyke swarm, South Africa. *Tectonophysics*, *583*,
629 145–157. https://doi.org/10.1016/J.TECTO.2012.10.035
630 Heilbronner, R. P. (1992). The autocorrelation function: an image processing tool for fabric
631 analysis. *Tectonophysics*, *212*(3), 351–370. https://doi.org/https://doi.org/10.1016/0040-
632 1951(92)90300-U
633 Hirt, A. M., Lowrie, W., Lüneburg, C., Lebit, H., & Engelder, T. (2004). Magnetic and mineral
634 fabric development in the Ordovician Martinsburg Formation in the Central Appalachian Fold
635 and Thrust Belt, Pennsylvania. *Geological Society, London, Special Publications*, *238*(1), 109–
636 126. https://doi.org/10.1144/GSL.SP.2004.238.01.09
637 Ho, N.-C., Peacor, D. R., & van der Pluijm, B. A. (1995). Reorientation mechanisms of
638 phyllosilicates in the mudstone-to-slate transition at Lehigh Gap, Pennsylvania. *Journal of*
639 *Structural Geology*, *17*(3), 345–356. https://doi.org/10.1016/0191-8141(94)00065-8
640 Ho, N.-C., Peacor, D. R., & Van Der Pluijm, B. A. (1996). Contrasting roles of detrital and
641 authigenic phyllosilicates during slaty cleavage development. *Journal of Structural Geology*,
642 *18*(5), 615–623. https://doi.org/10.1016/S0191-8141(96)80028-9
643 Hogan, P. J., & Burbank, D. W. (1996). Evolution of the Jaca piggyback basin and emergence of the
644 External Sierra, southern Pyrenees. In C. J. Dabrio & P. F. Friend (Eds.), *Tertiary Basins of*
645 *Spain: The Stratigraphic Record of Crustal Kinematics* (pp. 153–160). Cambridge: Cambridge
646 University Press. https://doi.org/DOI: 10.1017/CBO9780511524851.023
647 Houseknecht, D. W. (1984). Influence of grain size and temperature on intergranular pressure
648 solution, quartz cementation, and porosity in a quartzose sandstone. *Journal of Sedimentary*
649 *Research*, *54*(2), 348–361. https://doi.org/10.1306/212F8418-2B24-11D7-8648000102C1865D

650 Houseknecht, D. W. (1988). Intergranular pressure solution in four quartzose sandstones. *Journal of*
651 *Sedimentary Research*, *58*(2), 228–246. https://doi.org/10.1306/212F8D64-2B24-11D7-
652 8648000102C1865D
653 Housen, B. A., & van der Pluijm, B. A. (1991). Slaty cleavage development and magnetic
654 anisotropy fabrics. *Journal of Geophysical Research*, *96*(B6), 9937.
655 https://doi.org/10.1029/91JB00605
656 Izquierdo-Llavall, E., Aldega, L., Cantarelli, V., Corrado, S., Gil-Peña, I., Invernizzi, C., & Casas,
657 A. M. (2013). On the origin of cleavage in the Central Pyrenees: Structural and paleo-thermal
658 study. *Tectonophysics*, *608*, 303–318. https://doi.org/10.1016/J.TECTO.2013.09.027
659 Jähne, B. (1997). *Digital Image Processing: Concepts, Algorithms, and Scientific Applications*.
660 Berlin.
661 Kaestner, A., Lehmann, E., & Stampanoni, M. (2008). Imaging and image processing in porous
662 media research. *Advances in Water Resources*, *31*(9), 1174–1187.
663 https://doi.org/10.1016/J.ADVWATRES.2008.01.022
664 Kahl, W. A., Dilissen, N., Hidas, K., Garrido, C. J., LÓpez-SÁnchez-VizcaÍno, V., & RomÁn-
665 Alpiste, M. (2017). 3-D microstructure of olivine in complex geological materials
666 reconstructed by correlative X-ray μ-CT and EBSD analyses. *Journal of Microscopy*, *268*(2),
667 193–207. https://doi.org/10.1111/jmi.12598
668 Kanitpanyacharoen, W., Kets, F. B., Wenk, H.-R., & Wirth, R. (2012). Mineral Preferred
669 Orientation and Microstructure in the Posidonia Shale in Relation to Different Degrees of
670 Thermal Maturity. *Clays and Clay Minerals*, *60*(3), 315–329.
671 https://doi.org/10.1346/CCMN.2012.0600308
672 Ketcham, R. A. (2005). Three-dimensional grain fabric measurements using high-resolution X-ray
673 computed tomography. *Journal of Structural Geology*, *27*(7), 1217–1228.
674 https://doi.org/10.1016/J.JSG.2005.02.006
675 Ketcham, R. A., & Carlson, W. D. (2001). Acquisition, optimization and interpretation of X-ray
676 computed tomographic imagery: applications to the geosciences. *Computers & Geosciences*,
677 *27*(4), 381–400. https://doi.org/10.1016/S0098-3004(00)00116-3
678 Kristiansen, K., Valtiner, M., Greene, G. W., Boles, J. R., & Israelachvili, J. N. (2011). Pressure
679 solution – The importance of the electrochemical surface potentials. *Geochimica et*
680 *Cosmochimica Acta*, *75*(22), 6882–6892. https://doi.org/10.1016/J.GCA.2011.09.019
681 Labaume, P., Séguret, M., & Seyve, C. (1985). Evolution of a turbiditic foreland basin and analogy
682 with an accretionary prism: Example of the Eocene South-Pyrenean Basin. *Tectonics*, *4*(7),
683 661–685. https://doi.org/10.1029/TC004i007p00661
684 Launeau, P., Archanjo, C. J., Picard, D., Arbaret, L., & Robin, P.-Y. (2010). Two- and three-

685 dimensional shape fabric analysis by the intercept method in grey levels. *Tectonophysics*,
686 *492*(1), 230–239. https://doi.org/https://doi.org/10.1016/j.tecto.2010.06.005
687 Launeau, P., Bouchez, J.-L., & Benn, K. (1990). Shape preferred orientation of object populations:
688 automatic analysis of digitized images. *Tectonophysics*, *180*(2–4), 201–211.
689 https://doi.org/10.1016/0040-1951(90)90308-U
690 Launeau, P., & Cruden, A. R. (1998). Magmatic fabric acquisition mechanisms in a syenite: Results
691 of a combined anisotropy of magnetic susceptibility and image analysis study. *Journal of*
692 *Geophysical Research: Solid Earth*, *103*(B3), 5067–5089. https://doi.org/10.1029/97JB02670
693 Launeau, P., & Robin, P.-Y. F. (1996). Fabric analysis using the intercept method. *Tectonophysics*,
694 *267*(1–4), 91–119. https://doi.org/10.1016/S0040-1951(96)00091-1
695 Lee, J. H., Peacor, D. R., Lewis, D. D., & Wintsch, R. P. (1986). Evidence for syntectonic
696 crystallization for the mudstone to slate transition at Lehigh gap, Pennsylvania, U.S.A. *Journal*
697 *of Structural Geology*, *8*(7), 767–780. https://doi.org/https://doi.org/10.1016/0191-
698 8141(86)90024-6
699 Macente, A., Fusseis, F., Menegon, L., Xiao, X., & John, T. (2017). The strain-dependent spatial
700 evolution of garnet in a high-P ductile shear zone from the Western Gneiss Region (Norway): a
701 synchrotron X-ray microtomography study. *Journal of Metamorphic Geology*, *35*(5), 565–583.
702 https://doi.org/10.1111/jmg.12245
703 Meyer, E. E., Greene, G. W., Alcantar, N. A., Israelachvili, J. N., & Boles, J. R. (2006).
704 Experimental investigation of the dissolution of quartz by a muscovite mica surface:
705 Implications for pressure solution. *Journal of Geophysical Research: Solid Earth*, *111*(B8).
706 https://doi.org/10.1029/2005JB004010
707 Oertel, G. (1983). The relationship of strain and preferred orientation of phyllosilicate grains in
708 rocks—a review. *Tectonophysics*, *100*(1), 413–447.
709 https://doi.org/https://doi.org/10.1016/0040-1951(83)90197-X
710 Parés, J. M. (2015). Sixty years of anisotropy of magnetic susceptibility in deformed sedimentary
711 rocks . *Frontiers in Earth Science* . Retrieved from
712 https://www.frontiersin.org/article/10.3389/feart.2015.00004
713 Passchier, C. W., & Trouw, R. A. J. (2005). *Microtectonics*. Springer Berlin Heidelberg.
714 Perona, P., & Malik, J. (1990). Scale-space and edge detection using anisotropic diffusion. *IEEE*
715 *Transactions on Pattern Analysis and Machine Intelligence*, *12*(7), 629–639.
716 https://doi.org/10.1109/34.56205
717 Pfleiderer, S., & Halls, H. C. (1993). Magnetic pore fabric analysis: Verification through image
718 autocorrelation. *Journal of Geophysical Research: Solid Earth*, *98*(B3), 4311–4316.
719 https://doi.org/10.1029/92JB01851

720 Puigdefàbregas, C. (1975). La sedimentación molásica en la cuenca de Jaca. Retrieved from
721 http://hdl.handle.net/10261/82989
722 Ramachandran, G. N., & Lakshminarayanan, A. V. (1971). Three-dimensional Reconstruction from
723 Radiographs and Electron Micrographs: Application of Convolutions instead of Fourier
724 Transforms. *Proceedings of the National Academy of Sciences*, *68*(9), 2236–2240.
725 https://doi.org/10.1073/PNAS.68.9.2236
726 Renard, F., Ortoleva, P., & Gratier, J. P. (1997). Pressure solution in sandstones: Influence of clays
727 and dependence on temperature and stress. *Tectonophysics*, *280*(3–4), 257–266.
728 https://doi.org/10.1016/S0040-1951(97)00039-5
729 Russ, J., Neal, F., & Neal, F. B. (2015). *The Image Processing Handbook, Seventh Edition*. CRC
730 Press. https://doi.org/10.1201/b18983
731 Sayab, M., Miettinen, A., Aerden, D., & Karell, F. (2017). Orthogonal switching of AMS axes
732 during type-2 fold interference: Insights from integrated X-ray computed tomography, AMS
733 and 3D petrography. *Journal of Structural Geology*, *103*, 1–16.
734 https://doi.org/10.1016/J.JSG.2017.09.002
735 Sayab, M., Suuronen, J.-P., Hölttä, P., Aerden, D., Lahtinen, R., & Kallonen, A. P. (2015). High-
736 resolution X-ray computed microtomography: A holistic approach to metamorphic fabric
737 analyses. *Geology*, *43*(1), 55–58. https://doi.org/10.1130/G36250.1
738 Serra, J., & Vincent, L. (1992). An overview of morphological filtering. *Circuits Systems and Signal*
739 *Processing*, *11*(1), 47–108. https://doi.org/10.1007/BF01189221
740 Suuronen, J.-P., & Sayab, M. (2018). 3D nanopetrography and chemical imaging of datable zircons
741 by synchrotron multimodal X-ray tomography. *Scientific Reports*, *8*(1), 4747.
742 https://doi.org/10.1038/s41598-018-22891-9
743 Tarling, D., & Hrouda, F. (1993). *Magnetic anisotropy of rocks*. Springer Science & Business
744 Media.
745 Thissen, C. J., & Brandon, M. T. (2015). An autocorrelation method for three-dimensional strain
746 analysis. *Journal of Structural Geology*, *81*, 135–154.
747 https://doi.org/https://doi.org/10.1016/j.jsg.2015.09.001
748 Tournier, F. (2010). *Mécanismes et contrôle des phénomènes diagénétiques en milieu acide dans les*
749 *grès de l'Ordovicien glaciaire du bassin de Sbaa, Algérie*.
750 Underwood, E. E. (1970). Quantitative Stereology. Addison-Wesley Publishing Company.
751 van der Pluijm, B. A., Ho, N.-C., & Peacor, D. R. (1994). High-resolution X-ray texture
752 goniometry. *Journal of Structural Geology*, *16*(7), 1029–1032.
753 https://doi.org/https://doi.org/10.1016/0191-8141(94)90084-1
754 van der Pluijm, B. A., Ho, N.-C., Peacor, D. R., & Merriman, R. J. (1998). Contradictions of slate

formation resolved? *Nature*, *392*, 348. Retrieved from https://doi.org/10.1038/32810

Wenk, H.-R., Kanitpanyacharoen, W., & Ren, Y. (2017). Slate – A new record for crystal preferred orientation. *Journal of Structural Geology*. https://doi.org/10.1016/J.JSG.2017.12.009

Wenk, H.-R., Lonardelli, I., Franz, H., Nihei, K., & Nakagawa, S. (2007). Preferred orientation and elastic anisotropy of illite-rich shale. *Geophysics*, *72*(2), E69–E75. https://doi.org/10.1190/1.2432263

Weyl, P. K. (1959). Pressure solution and the force of crystallization: a phenomenological theory. *Journal of Geophysical Research*, *64*(11), 2001–2025. https://doi.org/10.1029/JZ064i011p02001

Zucali, M., Voltolini, M., Ouladdiaf, B., Mancini, L., & Chateigner, D. (2014). The 3D quantitative lattice and shape preferred orientation of a mylonitised metagranite from Monte Rosa (Western Alps): Combining neutron diffraction texture analysis and synchrotron X-ray microtomography. *Journal of Structural Geology*, *63*, 91–105. https://doi.org/10.1016/J.JSG.2014.02.011

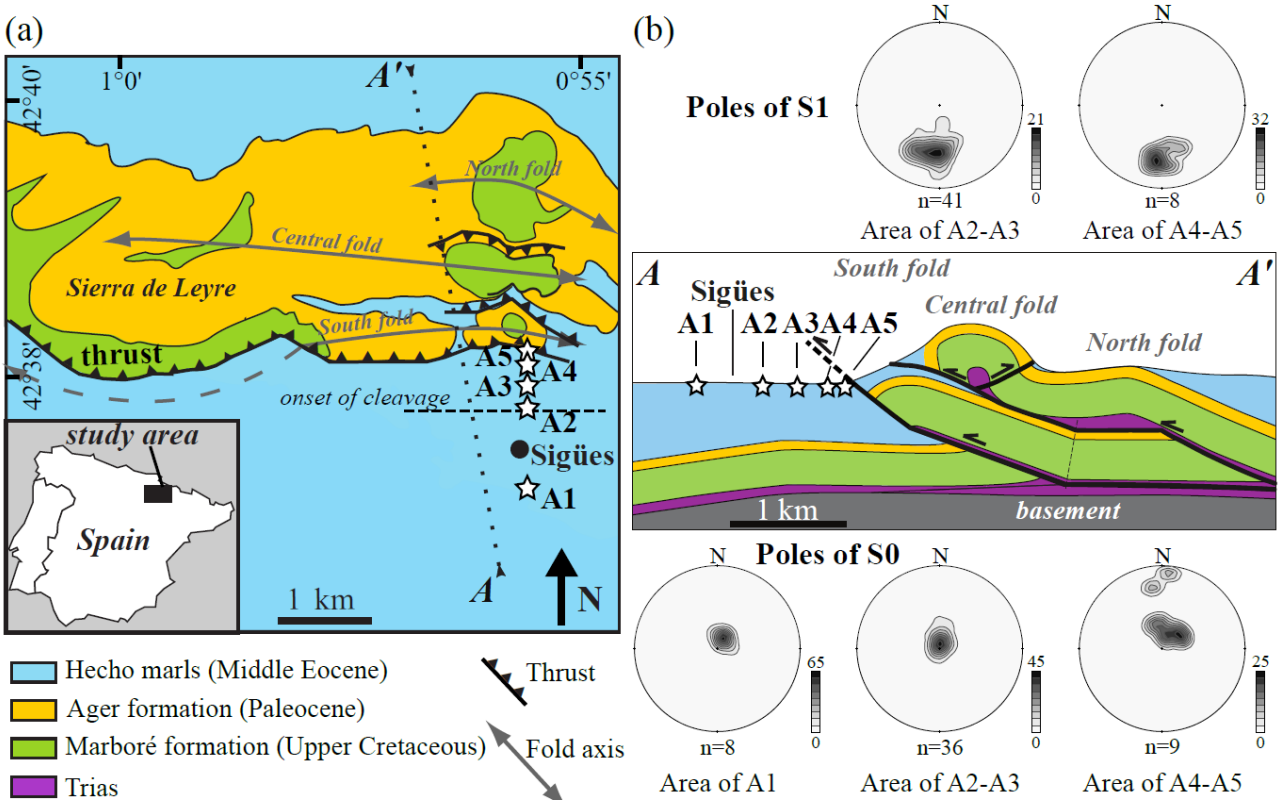

769

770 Fig. 1: (a) Simplified geological map between Sigües and Salvatierra in the Southern Pyrenees, Spain
771 (adapted from Puigdefàbregas (1975)). Sampling locations are indicated on the map. (b) North-south
772 cross-section corresponding to the A-A' profile on the geological map (adapted from Labaume et al.
773 (1985). Projected positions of the samples with respect to the cross-section are indicated. Poles of
774 bedding (S0) and cleavage (S1) measured in the field are reported onto equal area and lower
775 hemisphere projections using density contouring.

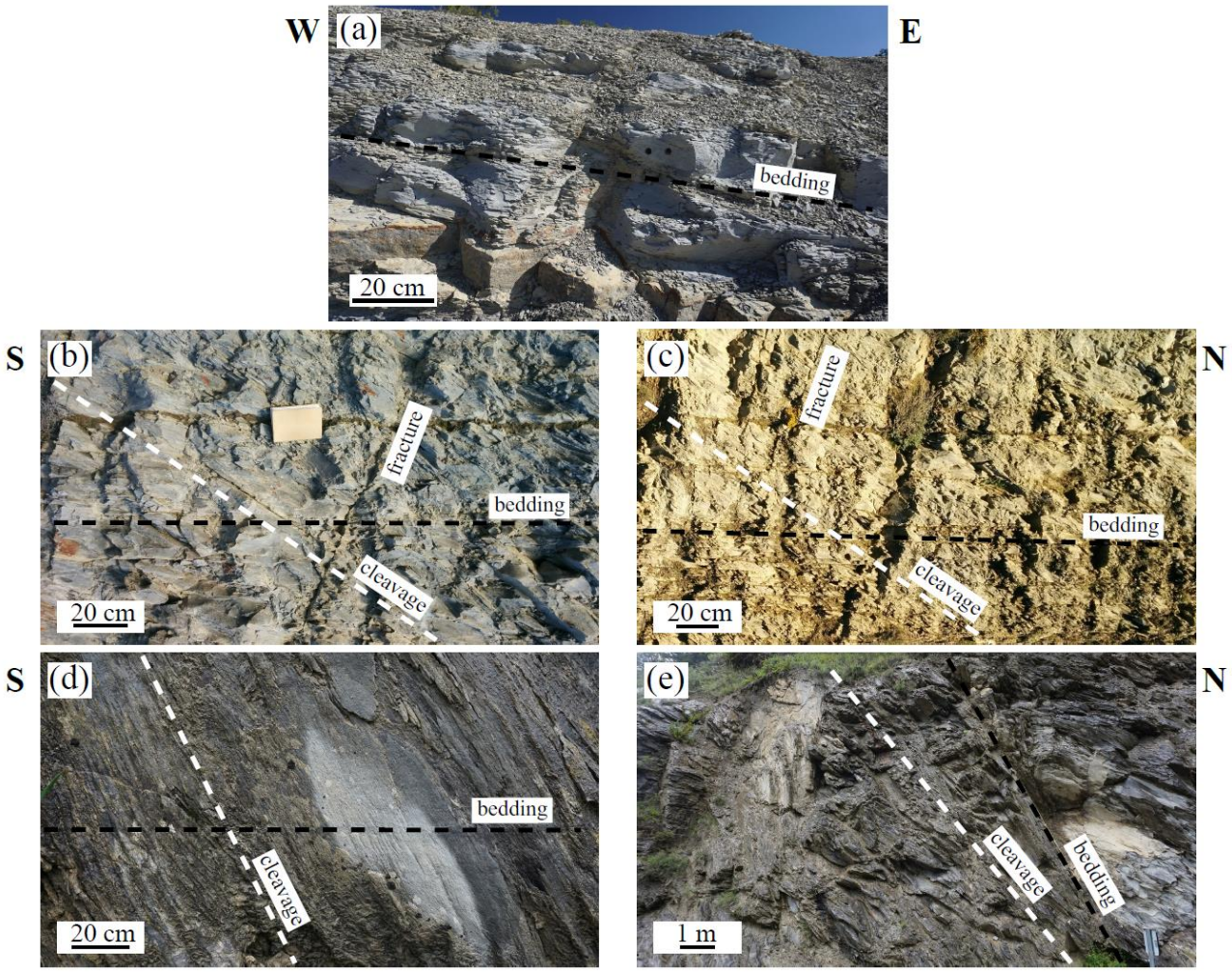

Fig. 2: Outcrop pictures of (a) cleavage-free domain (A1), (b) onset of cleavage (A2), (c) pencil-cleavage domain (A3), (d) slaty-cleavage domain with cleavage oblique to bedding (A4), (e) slaty-cleavage domain with superimposition of cleavage on bedding (A5). Distance from the thrust decreases from (a) to (e).

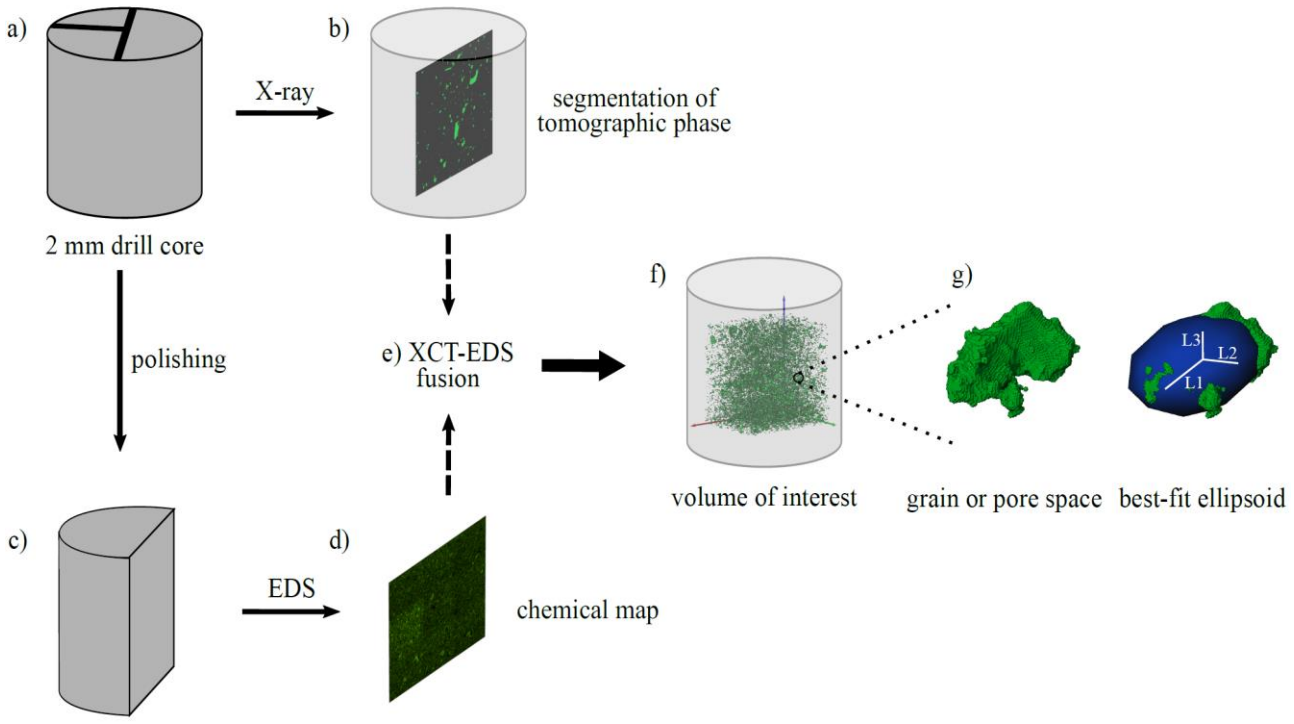

Fig. 3: Workflow of XCT-EDS combination method used in this study. a) drill core extracted from field sample with indication of the strike ('T' shaped marker on the top) measured in the field ; b) XCT acquisition followed by image processing to isolate phases of interest; c) drill core polishing for EDS analysis; d) chemical map obtained on the polished surface; e) data fusion corresponds to the registration of the XCT volume and the EDS map; f) selection of a volume of interest inside the XCT volume, each segmented tomographic phase is chemically identified; g) each grain or pore space in the volume of interest is approximated by a best-fit ellipsoid for shape fabric analysis ($L1 \geq L2 \geq L3$).

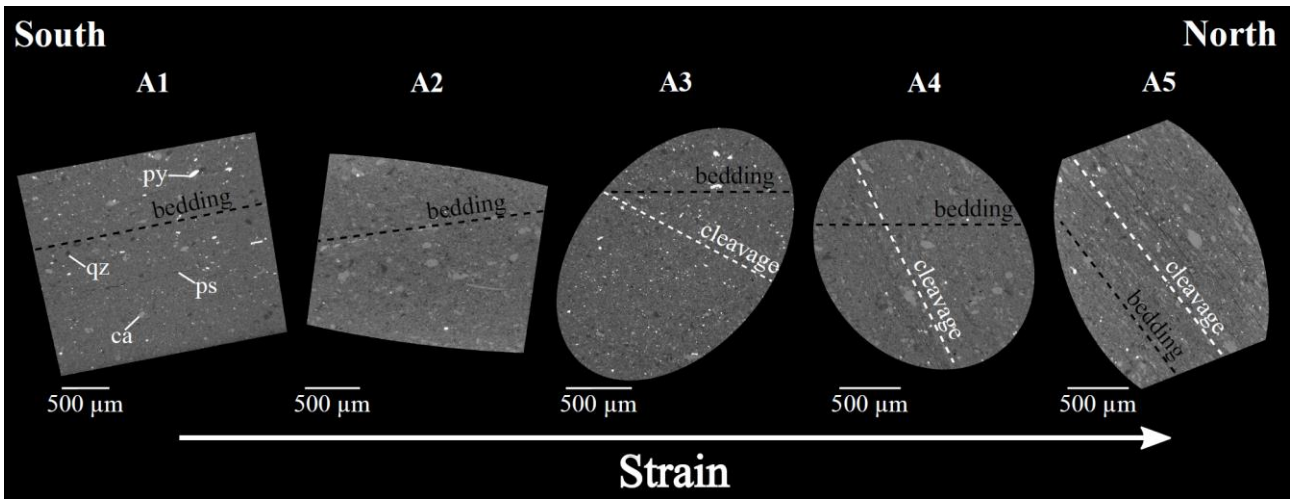

Fig. 4: XCT cross sections through the five samples (A1 to A5) in a common geographic coordinate system. The odd shape of the contours reflects that the presented north-south oriented plane intersects each cylindrical sample in a different way. Ca: calcite, ps: pore space, py: pyrite, qz: quartz. Strain intensity increases from A1 to A5. Cleavage and bedding planes in A5 are subparallel but cannot be differentiated.

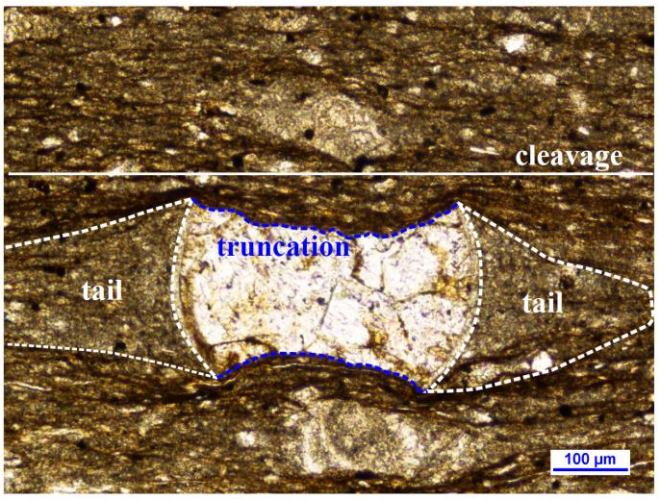

Fig. 5: Truncated calcite grain with pressure-shadows (tails) formed in the cleavage plane, observation by optical microscopy using in-plane-polarized transmitted light. Tails are filled by fine-grained calcite.

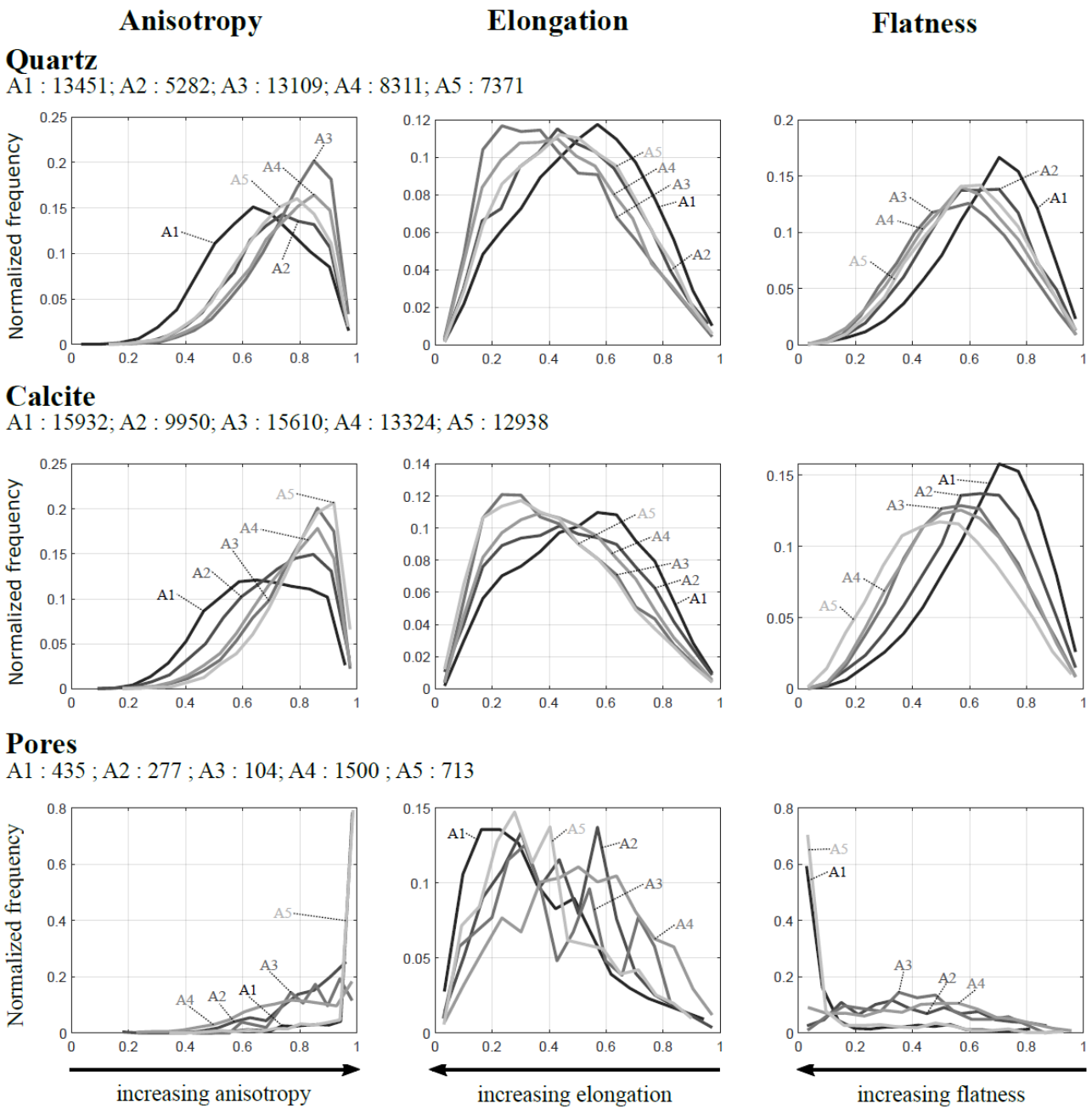

Fig. 6: Normalized histograms of anisotropy, elongation and flatness measured for quartz, calcite and pores in the five samples. Number of bins: 15. The number of considered objects in the samples is indicated below each subtitle.

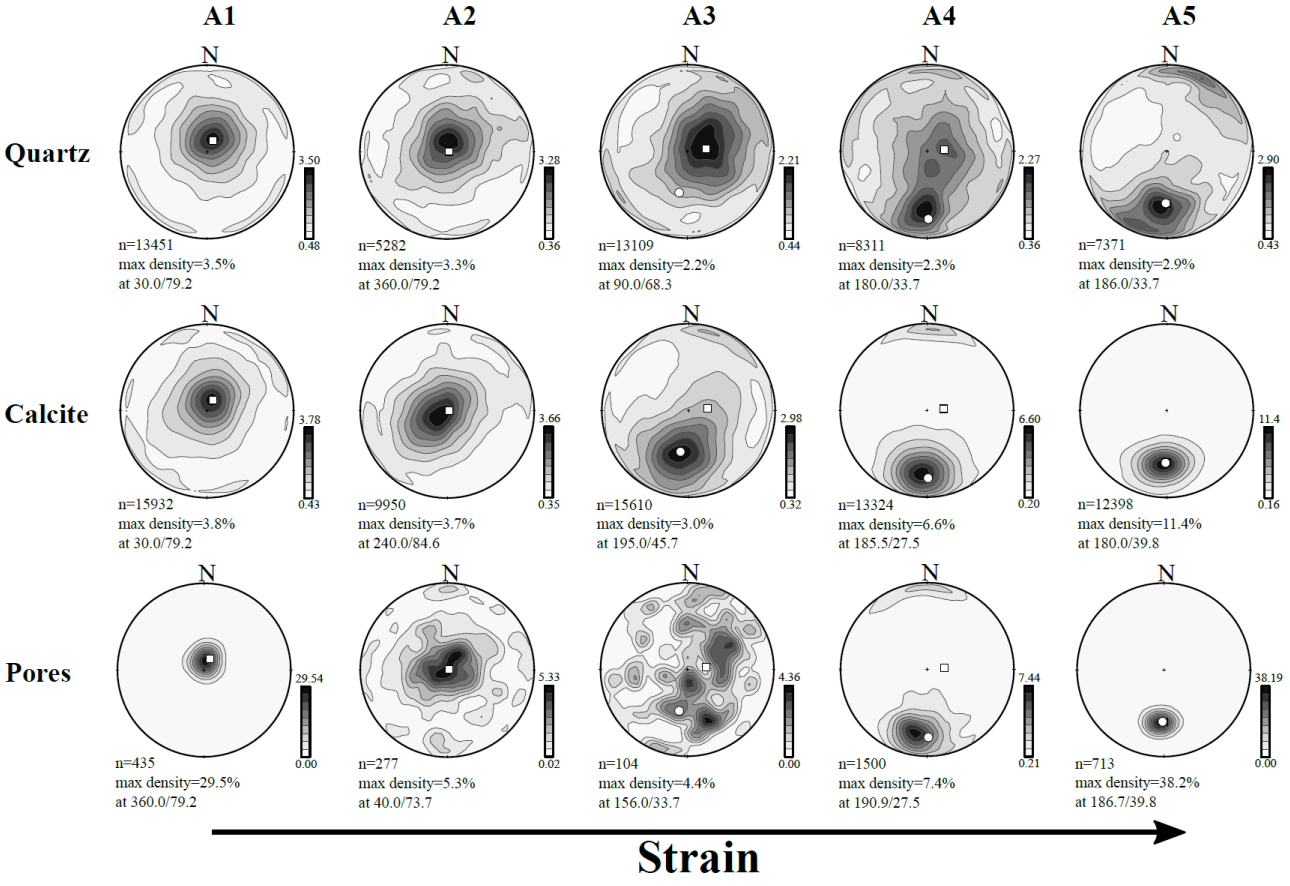

Fig. 7: Equal area and lower hemisphere projections of ellipsoids' short axes (L3) for quartz, calcite and pores in the five samples. White squares: pole of bedding; white circles: pole of cleavage. Note that in A5 the two poles are superimposed. The poles are deduced from the preferred alignment of grains in the XCT images. n: number of considered objects. Contours shown by gray scale in legends are indicated by %/1% area.

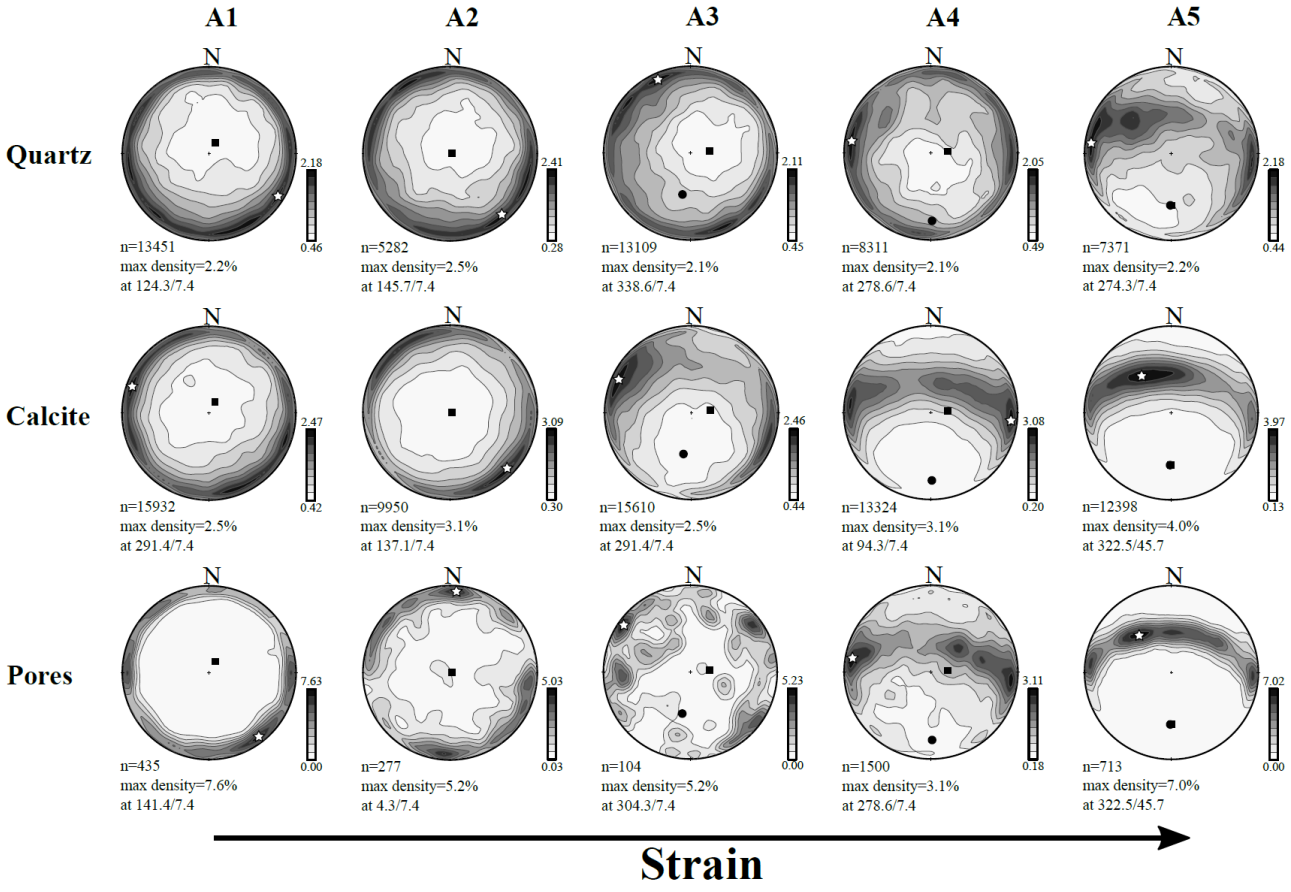

Fig. 8: Equal area and lower hemisphere projections of ellipsoids' long axes (L1) for quartz, calcite and pores in the five samples. Dark squares: pole of bedding; dark circles: pole of cleavage; white stars: maximum density. Note that in A5 the two poles are superimposed. The poles are deduced from the preferred alignment of grains in the XCT images. n: number of considered objects. Contours shown by gray scale in legends are indicated by %/1% area.

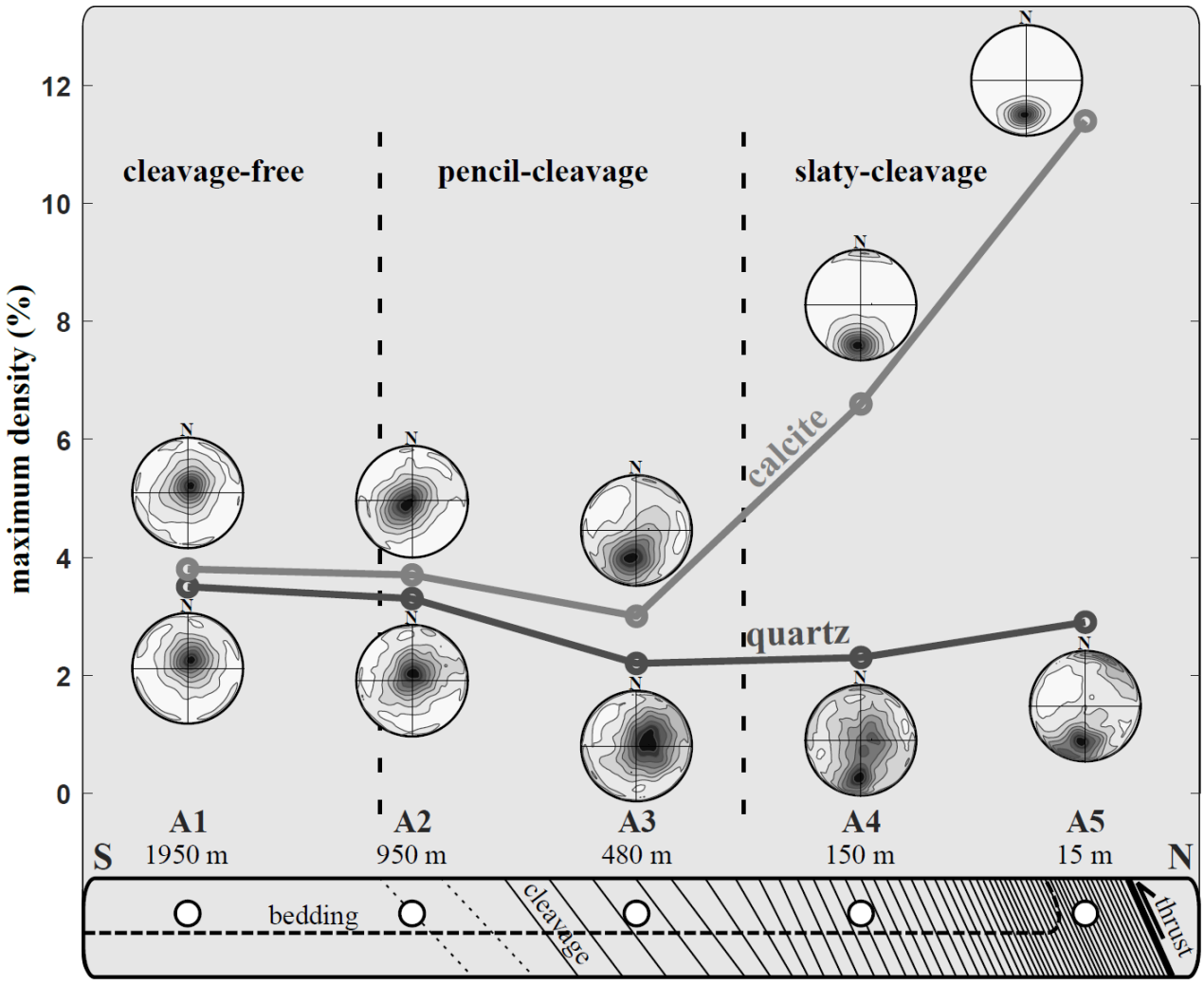

Fig. 9: Evolution of the maximum density of the pole of foliation showing contrasting SPO patterns of quartz and calcite across the section perpendicular to the thrust. At the bottom, the sample's distance from the thrust with indication of the orientation of bedding and cleavage planes is schematically represented.

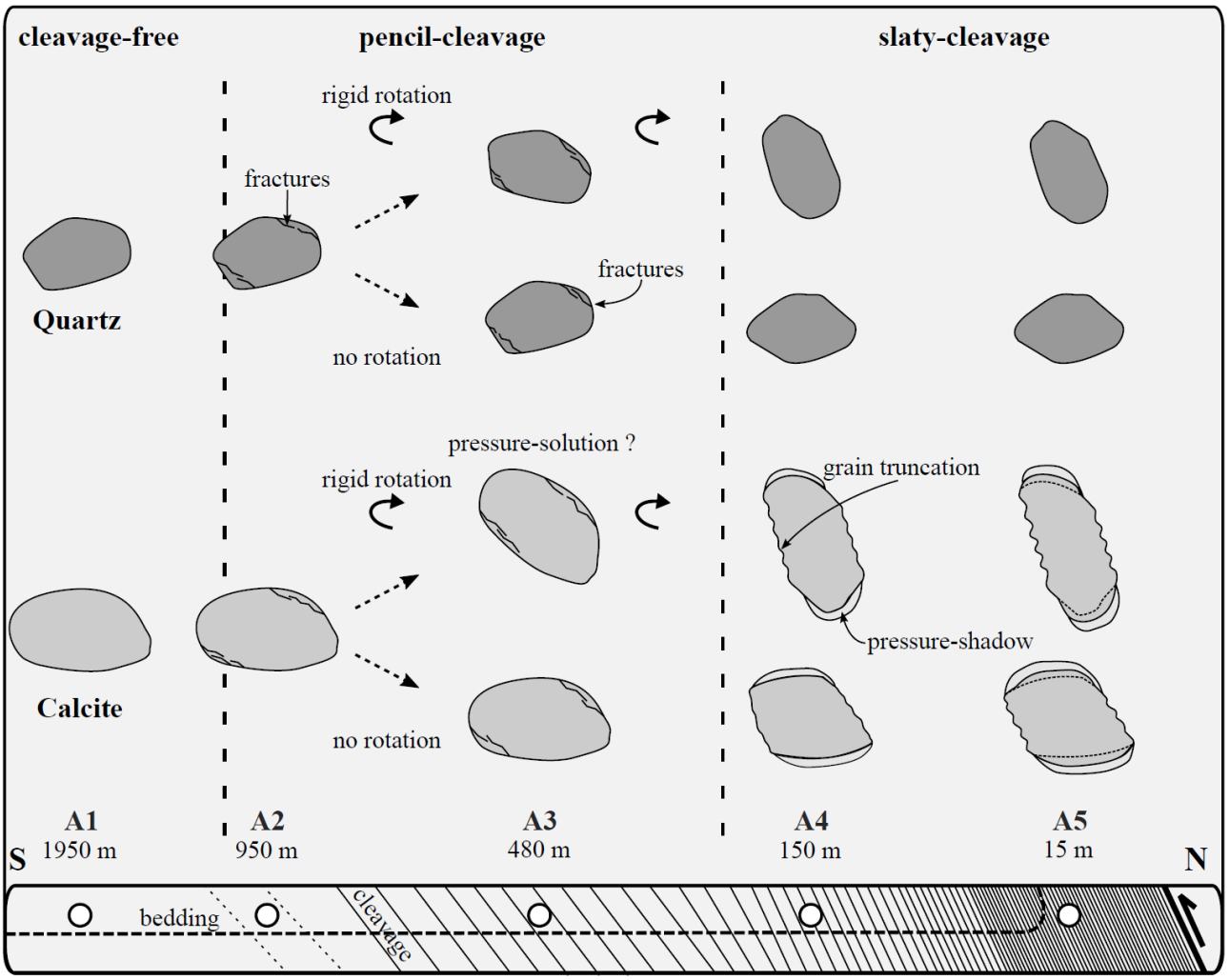

Fig. 10: Interpretative sketch of the dominant processes that affect the shape fabric of quartz and calcite in the matrix from the cleavage-free domain to the slaty-cleavage domain. Note that this sketch accounts for changes in grain SPO as changes in terms of their foliation. The sample's distance from the thrust is schematically represented at the bottom, with indication of the orientation of bedding and cleavage planes. For each type of grain (quartz or calcite), two scenarios are envisaged from A3 onwards, a first one featuring grain rotation and a second one without grain rotation. A1: no deformed grain; A2: grain fracturing; A3: grain fracturing, pressure-solution may occur; A4: no further deformation of quartz grain, pressure-solution of calcite grain; A5: no further deformation of quartz grain, enhanced pressure-solution of calcite grain.